Inhibition of GPX4 Induces the Death of p53-Mutant Triple-Negative Breast Cancer

William M. Tahaney
The University of Texas MD Anderson Cancer Center
Jing Qian
The University of Texas MD Anderson Cancer Center
Cassandra L. Moyer
The University of Texas MD Anderson Cancer Center
Nghi Nguyen
Texas A&M University
Amanda Lanier
The University of Texas MD Anderson Cancer Center
Yanxia Ma
The University of Texas MD Anderson Cancer Center
Jamal Hill
The University of Texas MD Anderson Cancer Center
Reid T. Powell
Texas A&M University
Clifford C. Stephan
Texas A&M University
Abhijit Mazumdar
The University of Texas MD Anderson Cancer Center
Peter J.A. Davies
Texas A&M University
Powel H. Brown (phbrown@mdanderson.org)
The University of Texas MD Anderson Cancer Center

Research Article

Keywords: TNBC, p53, GPX4, Ferroptosis, Gain-of-function

Posted Date: April 18th, 2022

DOI: https://doi.org/10.21203/rs.3.rs-1547583/v1

Abstract

Background

Triple-negative breast cancer (TNBC) is an aggressive subtype of breast cancer, characterized high rates of tumor protein 53 (p53) mutation and limited targeted therapies. Despite being clinically advantageous, direct targeting of mutant p53 has been largely ineffective. Therefore, we hypothesized that there exist pathways upon which p53-mutant TNBC cells rely upon for survival.

Methods

In vitro and *in silico* drug screens were used to identify drugs that induced preferential death in p53-mutant breast cancer cells. The effects of the glutathione peroxidase 4 (GPX4) inhibitor ML-162 was deleniated using growth and death assays, both *in vitro* and *in vivo*. The mechanism of ML-162 induced death was determined using small molecule inhibition and genetic knockout.

Results

High-throughput drug screening demonstrated that p53-mutant TNBCs are highly sensitive to peroxidase, cell cycle, cell division, and proteasome inhibitors. We further characterized the effect of the Glutathione Peroxidase 4 (GPX4) inhibitor ML-162 and demonstrated that ML-162 induces preferential ferroptosis in p53-mutant, as compared to p53-wild type, TNBC cell lines. Treatment of p53-mutant xenografts with ML-162 suppressed tumor growth and increased lipid peroxidation *in vivo*. Testing multiple ferroptosis inducers demonstrated p53-missense mutant, and not p53-null or wild type cells, were more sensitive to ferroptosis, and that expression of mutant *TP53* genes in p53-null cells sensitized cells to ML-162 treatment. Finally, we demonstrated that p53-mutation correlates with ALOX15 expression, which rescues ML-162 induced ferroptosis.

Conclusions

This study demonstrates that p53-mutant TNBC cells have critical, unique survival pathways that can be effectively targeted. Our results illustrate the intrinsic vulnerability of p53-mutant TNBCs to ferroptosis, and highlight GPX4 as a promising target for the precision treatment of p53-mutant triple-negative breast cancer.

Background

Triple-negative breast cancer (TNBC) is an aggressive subtype of breast cancer characterized by the absence of estrogen receptor (ER), progesterone receptor (PR), and human epidermal growth factor receptor 2 (HER2). TNBCs, representing 15–20% of all breast cancers, are associated with a younger age

of onset and with poorer survival in comparison to other subtypes, in part due to a current lack of broadly effective targeted therapies (1, 2). Though TNBCs exhibit a wide range of mutations in oncogenic and tumor suppressive proteins, one defining feature of TNBCs is the high frequency of mutations in Tumor Protein 53 (p53), with reported mutational frequencies between 80 and 90% (3). Known as the “guardian of the genome,” p53 plays crucial roles in the control of signals balancing cellular growth, survival, and death (4, 5). However, in the presence of p53 mutations, which most frequently occur in the DNA binding domain, cells lose the tumor suppressive functions of p53 and can gain oncogenic functions (6, 7). Given the prevalence of p53 mutations in TNBCs, and the critical role that p53 plays in growth and death regulation, it is evident that mutant p53 is an attractive therapeutic target.

Despite the high prevalence of p53 mutations in human cancers and their clinical significance, p53 mutations have been notoriously difficult to target in a clinical setting (8, 9). To date, there is only one drug that directly targets p53 mutations that has reached advanced clinical trials, APR-246 (Prima-1^{Met}, Eprenetapopt), and this trial failed to meet its primary endpoint in late 2020 (10). Therefore, there is an urgent need to identify drugs that that can target p53-mutant TNBCs. To overcome the challenges that come with directly targeting mutant p53, an alternative is to target other proteins or pathways that a mutant p53 cell may be reliant upon for survival. To this end, we hypothesized that specific proteins or pathways are critical for the survival of p53-mutant, but not p53-wild type breast cancers.

We conducted an integrated screen of small molecules with known protein targets to identify drugs that target specific vulnerabilities of p53-mutant breast cancer cells. This screen identified six compounds that induced preferential death or growth suppression in p53-mutant breast cancers, representing cell cycle, cell division, proteasome, and glutathione peroxidase inhibitors. Due to its effect against a large proportion of p53-mutant cell lines, and ability to induce death, we chose to further study the drug ML-162 and its protein target Glutathione Peroxidase 4 (GPX4). Through these studies we determined that inhibition of GPX4 exhibits highest efficacy in p53-mutant TNBCs, and that inhibition of GPX4 by small molecule or genetic knockout induces ferroptosis in these p53-mutant TNBCs. We further demonstrated that inhibition of GPX4 decreases the tumor burden of TNBCs *in vivo* and increases tumor lipid peroxidation. We determined p53-missense mutant, and not p53-null or wild type cells, were more sensitive to ferroptosis inducing drugs, and that expression of mutant *TP53* genes in TNBC cells sensitized these cells to ML-162 treatment. Finally, we determined that p53-mutant breast cancers exhibit high expression of the lipid enzyme Arachidonate 15-Lipoxygenase (ALOX15), that high ALOX15 correlates with poor patient prognosis, and that inhibition of ALOX15 rescues ML-162 mediated ferroptosis. These studies demonstrate that GPX4 is a promising target for the treatment of aggressive p53-mutant TNBCs, and highlight the ability of our screening technique to identify ways to target classically undruggable proteins, providing a foundation for identification of effective inhibitors of difficult to treat cancers.

Methods

Bioinformatics

Molecular Taxonomy of Breast Cancer International Consortium (METABRIC) and The Cancer Genome Atlas (TCGA) Breast datasets were accessed through cBioPortal (3,11–14). Area under the curve (AUC) values for cell lines were retrieved from the CTD^2 Data Portal (15,16). *TP53* mutational data was extracted from the Cancer Cell Line Encyclopedia (CCLE) portal (17).

Cell Lines and Culture Methods

Cal51 cells were obtained from DSMZ. Sum149PT cells were a generous gift from Naoto Ueno (MD Anderson, Houston, TX). All other cell lines were obtained from ATCC. Information for all cell lines and media compositions is found in **Supplemental Table 2**. For all Dox-inducible cell lines, regular FBS was replaced with Tet-system approved FBS (Clontech) in media. *TP53* DNA-resequencing of cell lines was performed with the help of the MD Anderson Advanced Technology Genomics (ATGC) core. All cell lines tested negative for mycoplasma, as assayed by PCR. Identities of cell lines were confirmed with short tandem repeat (STR) DNA fingerprinting, as previously described (18).

Generation of Dox-Inducible sgGPX4 Cell Lines

MDA-MB-468 iCas9 clones were generated previously by infection with Dox-inducible Lenti-Cas9 (Tet-on pCW-Cas9, Addgene plasmid #50661) (19). sgGPX4 and control constructs in the pCRISPR backbone were purchased from GeneCopoeia (HCC299543-SG01 and CCPCTR01, respectively). Cells were seeded in 60mm plates, then transfected with 2ug plasmid DNA and 6uL XtremeGENE 9 (Roche) in Opti-MEM (Invitrogen). Cells were selected with hygromycin for 7 days, after which all non-transfected cells had died. Resulting cells were screened for GPX4 knockout using western blot, and Cas9 expression was induced with doxycycline.

Generation of Dox-Inducible TP53-Mutant Cell Lines

TP53 cDNA was inserted into the pCR8/GW/TOPO vector (Invitrogen), then point mutagenized using the QuikChange Lightning II kit (Agilent) following the manufacturer's protocol. Primers were designed using QuikChange Primer Design Software (Agilent), and underlined amino acids represent the nucleic acid changed from wild type.

R248Q-F 5'-GAGGATGGGCCTCTGGTTCATGCCGCC-3'

R248Q-R 5'-GGCGGCATGAACCAGAGGCCCATCCTC-3'

R273H-F 5'-CAGGACAGGCACAAACATGCACCTCAAAGCTGTTC-3'

R273H-R 5'-GAACAGCTTTGAGGTGCATGTTTGTGCCTGTCCTG-3'

Resulting constructs were Gateway cloned into the pInducer20 vector, using LR Cloanse II (Invitrogen). Insertion of mutant TP53 into pInducer20 was confirmed with restriction digest mapping and DNA sequencing. Lentiviral vectors were prepared with co-transfection of viral helper plasmids pCMV-VSV-G

and pCMV-dr8.2 dvpr (Addgene plasmids #8454 and #8455, respectively) and transfected into HEK293T cells using X-tremeGENE (Roche). MDA-MB-436 cells were stably infected with viral media supplemented with polybrene for 48 hours, then selected with G418.

Drug Library

The drug library was curated from three separate libraries: the BROAD “Informer Set” of drugs as published by Seashore-Ludlow *et. al.* (16), the Texas A&M Institute for Biosciences and Technology’s Custom Clinical Library, and the Powel Brown Library, a collection of drugs targeting signaling pathways and nuclear receptors which are of interest to the Brown lab, totaling 453 unique drugs with known mechanisms of action. Drug annotations were manually curated and cataloged from databases or vendor sources and visualized using Protein Analysis Through Evolutionary Relationships (PANTHER) classification (20).

Method for High-Throughput *in Vitro* Drug Screening using an ATP Luminescence Assay

Briefly, cells were seeded in 384-well plates (Greiner), incubated at 37^{o}C for 24 hours, and treated with 10uM, 1uM, or 0.1 uM of each drug in duplicate with the aid of an Echo 550 and Access Workstation (Labctye) for 72 hours. As a surrogate for viability, ATP levels of treated cells were determined with CellTiterGlo (Promega) using an Infinite M1000pro plate reader (Tecan). All cell lines were screened twice with separate cell line passages, and screening fitness was determined with the screening window coefficient Z’.

In Vitro Drug Screen Data Processing

Data organization and analysis was performed using Pipeline Pilot (Biovia, 2018 Server edition) integrated with R. Raw cell counts were first normalized as the growth rate index (GR), purposed by Hafner et al., using the following equation:

$$GR = 2^{\left(\frac{x}{x_0}\right)} - 1, \text{ where } x = \log_2\left(\frac{\text{Drug}_{D_3}}{\text{Control}_{D_0}}\right) \text{ and } x_0 = \log_2\left(\frac{\text{Control}_{D_3}}{\text{Control}_{D_0}}\right)$$

wherein Drug D_3 is the value of drug treatment values, Control D_0 is the cell count values from a separate plate fixed on the day of drug addition, and Control D_3 is the on-plate negative control (21). The normalized growth rate versus concentration was then fit using a cascade of 6 different models to provide an optimal fit to a broad range of curve shapes. The first model tested attempted to fit normalized data to a hill slope (4-parameter logistic regression) using iteratively reweighted least squared method found in the robust R package (https://cran.r-project.org/web/packages/robust/robust.pdf). Failure to converge, defined by a threshold of 0.00001, results in the data being passed to a series of constrained logistic regression or linear models. The constrained models used are: a 3PL which either fixes the max and fits the minimum, slope, and EC50 or fixes the minimum and fits the max, slope, and EC50; a 2PL that

fixes the top and bottom to either the 2nd and 98th percentile or min and max of the dataset, respectively, and fits the slope and EC50; or a linear model if all other models fail. After curves were fit, the area under the curve (AUC) was calculated using numerical integration and subsequently normalized to the maximum theoretical value, which results in values between 0 (Full active) and 1 (in-active).

A cut point of AUC $\leq$ 0.5 in at least one p53-mutant cell line was required for the drug to progress into the counter screen. For the counter screen, a difference of > 0.1 between average p53 wild-type AUC and average p53-mutant AUC was considered a candidate *in vitro* drug.

Method for *in Silico* Drug Screening

Cancer Therapeutics Response Portal (CTRPv2.0) Informer Set AUC values were retrieved from the CTD^2 Data Portal and integrated with *TP53* mutational data extracted from the CCLE, representing 486 drugs. AUC values were normalized to the maximum theoretical value. A minimum cut point of AUC $\leq$ 0.5 in at least one p53-mutant cell lines was required for progression into the counter screen. Average AUC values of drugs that passed cut point were determined for p53 wild-type and p53-mutant breast cancer cell lines. A difference of > 0.1 between average p53 wild-type AUC and average p53-mutant AUC was considered a candidate *in silico* drug.

Cell Proliferation Assays of Breast Cancer Cell Lines

Cells were plated in 96-well plates (Nunc) incubated at 37^{o}C overnight, then treated with drugs at indicated concentrations for 72 hours. Plates were fixed with paraformaldehyde, stained with DAPI, and imaged with an ImageXpress Pico (Molecular Devices). Nuclei were segmented and counted by defining a threshold value of pixel intensity over background and object size, using the cell scoring algorithm of the CellReporterXpress Software (Molecular Devices). Results were either reported as fold growth or Hafner's growth rate. Resulting values were fit into logistic regression models using Prism 9.2 (GraphPad), from which IC50 and AUC values were extracted.

DRAQ7 Cell Death Assay of MDA-MB-468 Cells

MDA-MB-468 cells were plated in 96-well plates (Nunc), incubated at 37^{o}C overnight, and treated with indicated drugs for 24 hours. Cells were co-stained live with DRAQ7 (300nM) and Hoechst 33342 (10uM) for 20 minutes and imaged at 4X with an ImageXpress Pico (Molecular Devices), using DAPI and Cy5 filter cubes. Live and dead nuclei were segmented and counted by comparing pixel intensity to background and object size, using the cell scoring algorithm of CellReporterXpress Software (Molecular Devices).

Annexin V / PI Flow Cytometry

Cell lines were treated with DMSO, ML-162 (500nM, 24 hours), or staurosporine (1uM, 3 hours), then stained with Annexin-V and PI (Invitrogen) and prepared for flow cytometry analysis. Briefly, cells were washed with cold PBS, resuspended in Annexin V binding buffer, and incubated with FITC-conjugated

Annexin V and PI for 15 minutes. Cells were analyzed for Annexin V and PI intensity with a Gallios 561 (Beckman Coulter) with the help of the MD Anderson Flow Cytometry and Cellular Imaging Core.

Western Blotting

Western blots were performed as described previously (22). Primary antibodies were: GPX4 (Abcam, ab125066, 1:1000), TP53 (Santa Cruz, sc-126, 1:1000), Caspase 3 (Cell Signaling Technology, 14220, 1:1000), Caspase 7 (Cell Signaling Technology, 12872, 1:1000), Caspase 9 (Cell Signaling Technology, 9508, 1:1000), Actin (Sigma, SAB4301137, 1:4000), and Vinculin (Sigma, 05-386, 1:4000).

Brightfield Cell Imaging

Cells were seeded in 6-well plates in their respective media. Treatments and incubations were performed as indicated, following which cells were imaged live at 20X with an Eclipse Ti (Nikon) using NIS Elements Software v3.2 (Nikon).

Small Molecule Death Inhibition Assay

Cells were plated in 96-well plates (Nunc) and pre-treated with DMSO control or 10uM inhibitors Z-VAD-fmk, Necrostain-1, or Ferrostatin-1 (Cayman Chemical) for 24 hours, following which cells were treated with ML-162 with or without inhibitors for 72 hours. Plates were fixed, stained with DAPI, and imaged at 4x with an ImageXpress Pico (Molecular Devices). Nuclei were segmented and counted by comparing pixel intensity to background and object size, using the cell scoring algorithm of CellReporterXpress Software (Molecular Devices). Resulting nuclei counts were normalized with Hafner's growth rate metric.

C11-BODIPY$^{581/591}$ Fluorescent Imaging

Cells were seeded into 96-well optically clear black well plates (Nunc) and grown for 24 hours at 37^{o}C with or without FS-1. Cells were treated with 100nM ML-162, with or without FS-1 for 6 hours, then with 5uM C11-BODIPY581/591 (Molecular Probes) in HBBS for 30 minutes at 37^{o}C. Images were captured at 40X using an ImageXpress Pico (Molecular Devices) with FITC and TRITC filter cubes. Fluorescence intensity was calculated using CellReporterXpress Software (Molecular Devices).

Mouse Experiments

Experiments using nude mice (Jackson Laboratory) were performed with M.D. Anderson Institutional Animal Care and Use Committee (IACUC)-approved protocols. MDA-MB-468 or MDA-MB-231 cells were injected into the mammary fat pads of nude mice ($5x10^6$ or $7.5x10^5$ cells, respectively, per animal in 100µl PBS,). When tumors developed and reached approximately 50-100 mm^3, mice were randomized into groups to receive ML-162 (50mg/kg) or vehicle (DMSO), injected intratumorally 5 day per week. Tumor sizes were measured at indicated time points with digital calipers, and tumor volume was calculated with the formula: Volume = ($width^2$ x length)/2. Individual tumor growth rates were calculated with log-transformed linear regression.

H&E and Immunohistochemistry

Tumor samples were fixed using 4% paraformaldehyde and embedded in paraffin. Sections of tissue were mounted on slides and processed for immunohistochemical (IHC) staining, as previously described (23). For IHC staining, tissues were incubated with primary antibodies overnight at 4^{o}C: Lab Vision anti-Ki67 (Thermo Scientific, prediluted), anti-cleaved caspase 3 (Thermo Scientific, prediluted), or anti-4-hydroxynonenal (R&D Systems, 1:1000).

Data Analysis and Statistical Considerations

Z' was calculated as in Zhang *et al*. (24). A Z' of > 0.5 was required for each cell line replicate to be added to its respective primary or counter drug screen. Fold DRAQ7^{+} was calculated as the ratio between drug and DMSO control treated cell DRAQ7 percent positivities. Fold growth of cells was compared using a mixed-effects model with a Geisser-Greenhouse correction. Slopes of tumor growth were calculated with $\log_{10}$-transformed linear regression, then compared with Student's *t*-test. Kaplan-Meier curves were compared with log-rank analysis. All other experimental significance was determined with Student's *t*-test. For all experiments, a *p*-value of < 0.05 was considered statistically significant.

Results

Integrated High Throughput Drug Screening of Breast Cancer Cell Lines

To identify drugs that induce death or suppress growth of p53-mutant and not p53-wild type breast cancer cells, we performed an integrated high-throughput drug screen using *in vitro* and *in silico* drug screening (**Fig. 1A**). Our library totaled 453 unique compounds, with known and diverse mechanisms of action (**Fig. S1**and **Table S1**).

The *in vitro* screen began by examining the effect of the drug library on eight different p53-mutant TNBC cell lines. Cells were chosen for published *TP53*mutational status, which were then confirmed by DNA sequencing (**Table S2**). Drugs were screened at three concentrations using the ATP luminescence assay CellTiterGlo as a readout, yielding 67 drugs as capable of inducing death or suppressing growth in p53-mutant TNBC cell lines (**Fig. 1B, Fig. S2A-C**). We then counter-screened these 67 drugs against 5 individual p53-wild type breast and breast cancer cell lines using the same workflow as the primary screen. We determined the difference in drug-induced death or growth suppression between p53-mutant and p53-wild type cells by calculating the difference between average p53-mutant AUC and average p53-wild type AUC, wherein 13 drugs were identified as inducing preferential growth suppression or death induction of p53-mutant breast cancer cells (**Fig. 1C, Fig. S2D,Table S3**).

In addition to the *in vitro*drug screen, we mined the publicly available Cancer Therapeutics Response Portal dataset (CTRP v2.0, **Table S4**)[33]. We then integrated the breast cancer cell lines with their respective p53 mutational statuses using the Cancer Cell Line Encyclopedia (CCLE), listed in **Table S5**. Using this data, we examined the effect of the drug library against 19 separate p53-mutant breast cancer

cell lines, which identified 70 drugs as capable of inducing death or suppressing growth of p53-mutant breast cancer (**Fig. 1D, Fig. S2E-F**). We then conducted a counter screen of the 70 candidate drugs against 6 individual p53-wild type breast cancer cell lines, wherein we compared the average AUC values between p53-mutant and p53-wild type cell lines, which identified 18 drugs as preferentially inducing the death or suppressing the growth of p53-mutant breast cancer cells (**Fig. 1E, Table S6**).

To select drugs for further study, the candidate drugs from the *in vitro* and *in vitro*screens were integrated to identify shared protein targets and pathways with the aid of BioVenn(25). 6 drugs were identified in both *in vitro* and *in silico* screens (**Fig. 1F**). Of these drugs, there was one peroxidase inhibitor (ML-162), two cell cycle inhibitors (AZD7762 and MK-1775), one proteasome inhibitor (Ixazomib), and two cell division inhibitors (Docetaxel and SB-743921), as shown in **Figure 1G**. Drugs excluded after integration are listed in **Table S7**.

Identification of ML-162 as Inducing Preferential Death in p53-Mutant Triple-Negative Breast Cancer Cell Lines

To further examine our identified drug hits, we performed dose-response growth curves with p53-mutant and p53-wild type breast cancer cell lines (**Fig. 2A**). Using these curves, we compared the difference in AUC to determine the difference between growth-suppression and death-induction. As expected, four of our drugs – ML-162, AZD7762, MK-1775, and ixazomib –demonstrated a significant decrease of AUC in p53-mutant, as compared to p53 wild-type, cell lines (**Fig. 2B**). The remaining drugs, docetaxel and SB-743921, showed a non-significant decrease in AUC comparing p53-mutant and wild-type cells. We also compared differences in drug IC_{50} values and found ML-162 and MK-1775 to have a significant difference in IC_{50} between p53-mutant and p53-wild type breast cancer cell lines (**Fig. 2C**). Finally, we wanted to determine if our identified drugs were able to induce cell death. Using DRAQ7 and Hoechst co-staining, we determined that all drugs, with the exception of docetaxel, were able to induce cell death (**Fig. 2D**). As ML-162 induced the largest shift in AUC and IC_{50} values, and was also able to induce cell death, we chose to further characterize the effect of ML-162 and its target protein GPX4 on the survival of p53-mutant breast cancer.

GPX4 Expression Does Not Correlate with ML-162 Sensitivity.

As ML-162 is a direct inhibitor of GPX4, we sought to examine the expression of GPX4 in clinical datasets. Using METABRIC and TCGA datasets, we determined that TNBC tumors and *TP53*mutant tumors have lower mRNA expression of GPX4 than do non-TNBC tumors (**Fig. S3A**). We further examined the METABRIC dataset by PAM50 classification and found that basal and claudin-low subtypes expressed significantly lower levels of GPX4 (**Fig. S3B)**. This is consistent with expectations, as basal and claudin-low subtypes largely cluster with TNBC subtyping, and basal breast cancers have the highest rate of p53-mutations. However, when we examined the expression of GPX4 at the protein level, we did observe a difference in GPX4 expression comparing between p53-mutant and p53-wild type breast cancer cell lines (**Fig. S3C**). To determine if ML-162 sensitivity it due to altered GPX4 protein expression, we

performed a corraltion between GPX4 expression and ML-162 IC_{50} for breast cancer cell lines and determined there was not a significant correlation (**Fig. S3D**). Taken together, these data indicate that differences in ML-162 sensitivity are not due to GPX4 expression.

ML-162 Exhibits Potency in p53-Mutant TNBCs

To better understand how loss of GPX4 affects breast cancer cell lines of different histologic and p53-mutational subtypes, we determined the effect of ML-162 treatment on the growth of breast cancer cells in different subtypes. We determined that ML-162 did not have a significant effect on p53-wild type cell lines, regardless of subtype (**Fig 3A**). We then tested the effect of ML-162 on p53-mutant triple-negative breast cancer cells and observed a potent suppression of these cell lines (**Fig. 3B**). After one day of treatment, all p53-mutant TNBC cell lines had fold growth values below 1, suggesting ML-162 induced the death of these cells. In contrast, MCF10A, MCF7, ZR-75-1, and DU4475 cells did not exhibit a fold growth value below 1. We compared the differences in percent growth between DMSO and ML-162 in these cell lines and determined that only the p53-mutant TNBC cell lines exhibited a negative percent growth, providing further evidence of cellular death in these cells (**Fig 3C**). These data suggest that ML-162 exhibits preferential potencyin p53-mutant TNBCs when compared to p53-wild type breast and breast cancer cell lines.

GPX4 inhibition induces ferroptosis in triple-negative breast cancer

As ML-162 was able to induce cell death, we examined the effect of GPX4 inhibition in MDA-MB-468 cells on Annexin V positivity. Using staurosporine and DMSO as controls, we observed a highly significant induction of Annexin V positivity after treatment with ML-162 (**Fig. 4A)**. To

confirm this finding was not unique to MDA-MB-468 cells, we tested additional p53-mutant TNBC cell lines and determined that treatment with ML-162 significantly increased Annexin V positivity (**Fig S4A**). We then tested expression of cleaved caspases after staurosporine or ML-162 treatment to determine if this cell death was due to apoptosis. Interestingly, ML-162 treatment did not induce these traditional apoptotic death markers (**Fig. 4B**). We then examine the cellular morphology after staurosporine or ML-162 treatment. While staurosporine-treated cells exhibited the characteristic cell shrinkage and membrane blebbing, ML-162 treated cells were observed to be markedly enlarged (**Fig. 4C, Fig. S4B**).

To determine the mechanism of cell death induced by ML-162, we co-treated p53-mutant TNBC cells with ML-162 and small molecule inhibitors of cell death, including Z-VAD(OMe)-FMK (Z-VAD, apoptosis inhibitor), Necrostatin-1 (Nec-1, necrosis inhibitor), and Ferrostatin-1 (FS-1, ferroptosis inhibitor). FS-1 was able to most potently reduce sensitivity to ML-162, indicating that ML-162 induces ferroptosis in p53-mutant TNBC cell lines (**Fig. 4D**). As ML-162 is reported to be an inhibitor of GPX4, we used CRISPR-Cas9 technology to create an inducible GPX4 knockout cell line to confirm the on-target effect of ML-162 (**Fig. S5A**). We determined that Dox-treatment of sgGPX4 cells induced death, whereas Dox treatment of control cells did not (**Fig. S5B**). We then examined the morphology of these cells with and without GPX4 knockout using brightfield microscopy and determined that GPX4 knockout cells exhibited the same

cellular phenotype as ML-162 treated cells (**Fig. S5C**). Finally, we tested whether treatment with FS-1 could rescue the death induction of GPX4 knockout. As shown in **Fig. 5E**and **Fig. S5D**, Dox-treated GPX4 knockout cells died, while cotreatment with Dox/FS-1 rescued the lethality of GPX4 knockout, demonstrating that loss of GPX4 in p53-mutant TNBCs induces ferroptosis.

To further confirm this induction of ferroptosis, we used the fluorescent lipid peroxidation probe C11-BODIPY$^{581/591}$ to image cells after ML-162 treatment or GPX4 knockout. C11-BODIPY$^{581/591}$ is oxidized through lipid peroxidation, upon which its excitation spectra shift from red to green. Treatment with DMSO or FS-1 results in low levels of C11 oxidation, whereas ML-162 treatment yielded a significant induction of C11 oxidation, which was reversed upon co-treatment with FS-1 (**Fig. 4F**). To cofirm this finding was not exclusively in MDA-MB-468 cells, we tested three additional p53-mutant TNBC and again observed that ML-162 induces C11-BODIPY$^{581/5}$ oxidation, which is ablated with FS-1 co-treatment (**Fig. S4C**). Collectively, these data demonstrate that inhibition of GPX4 in p53-mutant TNBCs results in ferroptosis.

ML-162 Suppresses *in Vivo*p53-Mutant TNBC Xenograft Growth

In order to determine the effect of GPX4 inhibition on *in vivo*, we tested the effect of ML-162 in p53-mutant TNBC xenografts. MDA-MB-468 cells were injected into mammary fat pads and randomized into two treatment groups when tumors were approximately 100mm^3, then treated five times weekly with intratumoral vehicle or 50mg/kg ML-162 and growth curves of individual tumors were plotted for vehicle and ML-162 treated tumors. As demonstrated in **Fig. 5A**,tumor growth is slower in ML-162 treated MDA-MB-468 tumors than in vehicle treated tumors, indicating that ML-162 has *in vivo* efficacy. As tumor growth was roughly exponential, tumor volumes were $\log_{10}$ transformed and fit with linear regression to determine the slope of tumor growth. When compared, there was a significant decrease in the growth rate of tumors treated with ML-162 compared to vehicle (**Fig. 5B**). To confirm these findings can be replicated in multiple p53-mutant TNBC cell lines, we also tested the effect of ML-162 on MDA-MB-231 xenografts. As in MDA-MB-468 xenografts, we observed a significant reduction of tumor burden in ML-162 treated cells compared to vehicle (**Fig. 5C-D**).

We then analyzed MDA-MB-231 tumors with immunohistochemistry (**Fig. 5C-D**). To determine the effect on cell proliferation, we compared expression of Ki67 in these tumors, which was not significantly different between groups. We next examined the induction of apoptosis using cleaved caspase 3, which was found to not exhibit significant differences. Finally, to confirm that *in vivo* activity of ML-162 was due to ferroptosis, we determined the level of 4-hydroxynonenal (4-HNE), a ferroptosis byproduct, in ML-162 xenograft treated tumors using immunohistochemistry. Upon examination, we determined that 4-HNE was significantly increased in ML-162 treated tumors when compared to vehicle treatment. These results demonstrate that ML-162 is capable of decreasing p53-mutant TNBC xenograft burdens by inducing ferroptosis in these tumors.

Expression of Missense-Mutant p53 Sensitizes Cells to Ferroptotic Induction.

To further examine the role of p53 mutational status in ferroptotic sensitivity, we tested ML-162 and three additional ferroptosis inducing compounds – GPX4 inhibitors ML-210 and *1S-3R*-RSL3 and System X_c inhibitor erastin – against a panel of p53-missense mutant, p53-null, and p53-wild type breast cancer cells (**Fig. 6A**). We quantified differences in these dose-response curves by analyzing both AUC (**Fig. 6B**) and drug IC_{50} (**Fig. 6C**).In both quantifications p53-missense mutant TNBCs were more sensitive to all compounds than were the p53-wild type and, surprisingly, p53-null breast cancer cell lines, indicating this sensitivity may be due to a mutant p53-gain of function effect. To determine if expression of mutant p53 was sufficient to induce sensitivity to GPX4 inhibition, we created a series of inducible p53-mutants in the p53-null TNBC cell line MDA-MB-436. These cell lines express a mutant *TP53*gene for the hotspot mutations p53-R248Q and p53-R273H upon addition of Dox (**Fig. 6D**). To determine how expression of this mutant gene altered sensitivity to ML-162 treatment, we treated the cells with Dox, and then determined their growth in the presence of ML-162. As demonstrated in **Fig 6E**, expression of either p53-R248Q or p53-R273H was sufficient to sensitize TNBC cells to GPX4 inhibition. These data collectively demonstrate that p53 missense mutant TNBCs are sensitive to ferroptosis, and this sensitivity is governed in part by p53-mutational status.

ALOX15 Expression Correlates with TP53-Mutational Status and ML-162 Sensitivity in TNBC

Ferroptosis is reliant upon lipid metabolism. Given that p53-mutant TNBC cells exhibit increased sensitivity to ferroptosis, but p53-mutational status does not significantly alter GPX4 protein expression, we sought to determine if expression of other critical enzymes for ferroptotic lipid metabolism was altered. We examined the lipoxygenase Arachidonate 15-Lipoxygenase (ALOX15) for its biologic role in producing lipid hydroperoxides (LOOH) from lipids (LH) (**Fig 7A**). Using publically available TCGA breast data, we determined that ALOX15 was uniquely increased in missense mutants, but not in truncating mutations (**Fig 7B**). We additionally determined that patients with high expression of ALOX15 had a significantly worse prognosis (**Fig 7C**). As ALOX15 expression was highest in p53-missense mutant samples, we examined whether ALOX15 expression was prognostic for survival based on p53-mutational status.

As ALOX15's role in the synthesis of polyunsaturated lipid hydroperoxides may promote ferroptosis, we hypothesized that inhibition of ALOX15 would reverse the death-inductive effect of ML-162. To test this, we co-treated cells with ML-162 and the ALOX15 small molecule inhibitor PD-146176. Addition of PD-146176 was able to significantly rescue ML-162-induced death in three p53-muatnt TNBC cell lines, indicating that ALOX15 expression or activity positively correlates with sensitivity to ferroptosis (**Fig 7D**). These data suggest ALOX15 is highly expressed in *TP53*-missense mutant breast cancer and highlights the importance of lipid pathways in *TP53*-missense mutant breast cancer.

Discussion

In this study, we identified multiple proteins and pathways critical for the growth and survival of p53-mutant breast cancer. We further studied the GPX4 inhibitor ML-162 and demonstrated ML-162 induced

preferential death in p53-mutant triple-negative breast cancers. Through both small molecule inhibition and genetic knockout, this death induction was demonstrated to occur through ferroptosis. *In vivo*, GPX4 inhibition was shown to decrease growth of p53-mutant TNBC xenografts and induce ferroptosis. Furthermore, p53-missense mutant cells were found to be more sensitive to ferroptotic induction than p53-null or wild type cells, and that expression of a mutant *TP53* gene was sufficient to sensitize TNBC cells to ML-162. Finally, this study highlighted that p53-missense mutant TNBCs harbor increased expression of the oxidoreductase ALOX15, and that ALOX15 expression correlates with sensitivity to ferroptosis.

Our proposed model for the role of GPX4 in breast cancer is shown in Fig. 7E. In p53-wild type non-TNBC breast cancer, cells exhibit low levels of ALOX15, resulting in low levels of lipid hydroperoxide (LOOH) production. These LOOH are reduced to LOH via GPX4, preventing the formation of lipid radicals ($LO^{\cdot}$). Upon GPX4 inhibition, LOOH become $LO^{\cdot}$, but does not reach a level sufficient to induce ferroptosis. In p53-mutant TNBC cells, there is a higher level of ALOX15, producing a greater level of LOOH. Upon GPX4 inhibition, this results in a large generation of $LO^{\cdot}$, which induces ferroptosis and subsequent death.

In addition to ferroptosis, this paper highlights other molecular vulnerabilities of p53-mutant triple negative breast cancer, including proliferation, cell division, and protein turnover. Cell proliferation inhibitors AZD7762 and MK-1775, cell cycle checkpoint kinase and WEE1 kinase inhibitors, respectively, have been previously demonstrated to regulate survival of p53-mutant cancers (26–29). These kinases function at the G2/M checkpoint, the sole checkpoint for DNA repair in p53-mutant cancers (30). We also identified cell division inhibitors, such as the microtubule inhibiting chemotherapy agent docetaxel and KIF11 inhibitor SB-743921, as preferentially effective in p53-mutant breast cancers. Both of these inhibit cell division, causing accumulated DNA damage and further highlighting the importance of DNA damage repair in the G2 phase of the cell cycle. Finally, we identified the proteasome inhibitor ixazomib as having greater activity in p53-mutnat breast cancers. The effect of proteasome inhibition in p53-mutant cancers is still unclear, with some reports stating effect from proteasome inhibitors is p53-independent, while others share our findings of a mutant p53 dependent activity (31–35).

While studies have been conducted on the effect of GPX4 inhibition and ferroptotic induction in various cancer subtypes, the specific role of p53-mutation in the sensitivity of triple-negative breast cancer to ferroptosis has not previously been known. A recent publication showed basal breast tumors are more sensitive to ferroptotic induction than are ER-positive cells, but did not explore the role of p53 in this finding (36). Similarly, Thompson *et al.* demonstrated that different *TP53* mutations can increase sensitivity to ferroptosis, though no clear mechanism linking *TP53* mutation and ferroptosis was demonstrated (37). The most well-studied mechanism linking p53-mutant status and ferroptosis was proposed by Liu *et al.*, where it was demonstrated mutant p53 can entrap NRF2 and subsequently repress *SLC7A11* expression in esophageal cancers, resulting in ferroptosis (38). Future studies will be needed to determine the downstream effects of *TP53* mutational status on lipid family member expression and ferroptosis-related gene expression in the context of both breast cancer and other p53-mutant cancers.

Overall, these studies demonstrate that alterations in the activity of GPX4 and potentially other lipid metabolizing enzymes lead to ferroptosic sensitivity in p53-mutant cancers.

Conclusions

For this study, we conducted an integrative high-throughput drug screen and demonstrated that p53-mutant breast cancer cells, but not p53-wild type breast cancer cells, are sensitive to ferroptosis inducers, as well as proteasome, cell cycle, and cell division inhibitors. The GPX4 inhibitor ML-162 induces death of p53-mutant TNBC cells through ferroptosis, demonstrating that GPX4 is critical for the survival of p53-mutant TNBC and provides a strategy to target these highly aggressive cancers. Finally, this study highlights a drug screening strategy to identify vulnerabilities of classically undruggable targets, laying a foundation for the identification of additional targets for more effective treatment of triple-negative breast cancer.

Abbreviations

4-HNE	4-Hydroxynonenal
ALOX15	Arachidonate 15-Lipoxygenase
AUC	Area Under the Curve
CCLE	Cancer Cell Line Encyclopedia
ER	Estrogen Receptor
FS-1	Ferrostatin-1
GPX4	Gluathione Peroxidase 4
HER2	Human Epidermal Growth Factor Receptor 2
LH	Lipid
$LO^{\cdot}$	Lipid Radical
LOH	Lipid Alcohol
LOOH	Lipid Hydroperoxide
METABRIC	Molecular Taxonomy of Breast Cancer International Consortium
Nec-1	Necrostatin-1
P53	Tumor Protein 53

PANTHER	Protein Analysis Through Evolutionary Relationships
PR	Progesterone Receptor
STR	Short Tandem Repeat
TCGA	The Cancer Genome Atlas
TNBC	Triple-Negative Breast Cancer
Z-VAD	Z-VAD(OMe)-FMK

Declarations

Ethics approval and consent to participate – All animal experiments were performed using protocols approved by the M.D. Anderson Institutional Animal Care and Use Committee (IACUC).

Consent for publication – Not applicable

Availability of data and materials – mRNA expression of METABRIC and TCGA Breast Datasets are available at https://www.cbioportal.org. PANTHER classifications are available from www.pantherdb.com. CTD^2 Data Portal is found at https://ocg.cancer.gov/programs/ctd2/data-portal. CCLE mutational data are available at https://portals.broadinstitute.org/ccle. Additional data supporting the findings are available within the article, and from the corresponding author on reasonable request.

Competing interests – P. Brown served as a Scientific Advisory Board Member for the Susan G. Komen for the Cure Foundation (until 2017), and Dr. Brown is a holder of GeneTex stock (less than 1% of the total company stock); neither of these relate to this publication. All remaining authors declare no actual, potential, or perceived conflict of interest that would prejudice the impartiality of this article.

Funding – This work was funded by a CPRIT Core Grant (RP150578, N.N., R.T.P, C.C.S., P.J.A.D.), an NCI Core Grant (CA016672), a Susan G Komen Promise Grant (KG081694, P.H.B.), a Komen SAB grant (KG081694, P.H.B.), and the Charles Cain Endowment grant (P.H.B.).

Authors' Contributions – WMT: Conceptualization, data curation, conduction of experiments, formal analysis, methodology, manuscript writing, and manuscript editing. **JQ:** Conduction of experiments, formal analysis, methodology, manuscript writing, manuscript editing. **CLM:** Conduction of experiments, formal analysis, manuscript editing. **NN:** Conduction of experiments, methodology, manuscript editing. **AL:** Conduction of experiments, methodology, manuscript editing. **YM:** Methodology, manuscript editing. **JH:** Conduction of experiments, methodology, manuscript editing. **RTP:** Resources, conceptualization, data curation, conduction of experiments, formal analysis, methodology, and manuscript editing. **CCS:** Resources, conceptualization, methodology, and manuscript editing. **AM:** Conceptualization, data curation, conduction of experiments, formal analysis, methodology, manuscript writing, and manuscript

editing. **PJAD:** Resources, conceptualization, methodology, and manuscript editing. **PHB:** Resources, conceptualization, methodology, manuscript writing, and manuscript editing.

Acknowledgments – We would like to thank Sam Short and Michelle Savage for assisting in the submission. We additionally thank CPRIT, the NCI, and the Susan G Komen Foundation for the financial support of this research.

References

1. Perou CM, Sørlie T, Eisen MB, van de Rijn M, Jeffrey SS, Rees C a, et al. Molecular portraits of human breast tumours. Nature. 2000;406(6797):747–52.
2. Yin L, Duan JJ, Bian XW, Yu SC. Triple-negative breast cancer molecular subtyping and treatment progress. Breast Cancer Res. 2020;22(1):1–13.
3. Pereira B, Chin S, Rueda OM, Vollan HM, Provenzano E, Bardwell HA, et al. The somatic mutation profiles of 2,433 breast cancers refine their genomic and transcriptomic landscapes. Nat Commun. 2016;7(May):1–15.
4. Lane DP. p53, guardian of the genome. Vol. 358, Nature. 1992. p. 15–6.
5. Strachan T, Read AP. Chapter 18: Cancer Genetics. In: Human Molecular Genetics 2. 2nd ed. New York, NY: Wiley-Liss; 1999.
6. Soussi T, Wiman KG. TP53: An oncogene in disguise. Cell Death Differ. 2015;22(8):1239–49.
7. Zhang C, Liu J, Xu D, Zhang T, Hu W, Feng Z. Gain-of-function mutant p53 in cancer progression and therapy. J Mol Cell Biol. 2020;12(9):674–87.
8. Duffy MJ, Synnott NC, McGowan PM, Crown J, O'Connor D, Gallagher WM. P53 as a target for the treatment of cancer. Cancer Treat Rev. 2014;40(10):1153–60.
9. Hu J, Cao J, Topatana W, Juengpanich S, Li S, Zhang B, et al. Targeting mutant p53 for cancer therapy: direct and indirect strategies. J Hematol Oncol. 2021;14(1):1–19.
10. Sallman D. NCT037457169: APR-246 & Azacitidine for the Treatment of TP53 Mutant Myelodysplastic Syndromes (MDS). 2021.
11. Cerami E, Gao J, Dogrusoz U, Gross BE, Sumer SO, Aksoy BA, et al. The cBio Cancer Genomics Portal: An open platform for exploring multidimensional cancer genomics data. Cancer Discov. 2012;2(5):401–4.
12. Gao J, Aksoy BA, Dogrusoz U, Dresdner G, Gross B, Sumer SO, et al. Integrative Analysis of Complex Cancer Genomics and Clinical Profiles Using the cBioPortal Complementary Data Sources and Analysis Options. Sci Signal. 2014;6(269):1–20.
13. Curtis C, Shah SP, Chin S-F, Turashvili G, Rueda OM, Dunning MJ, et al. The genomic and transcriptomic architecture of 2,000 breast tumours reveals novel subgroups. Nature. 2012;486(7403):346–52.

14. Ciriello G, Gatza ML, Beck AH, Wilkerson MD, Rhie SK, Pastore A, et al. Comprehensive Molecular Portraits of Invasive Lobular Breast Cancer. Cell. 2015;163(2):506–19.
15. Basu A, Bodycombe NE, Cheah JH, Price E V., Liu K, Schaefer GI, et al. An interactive resource to identify cancer genetic and lineage dependencies targeted by small molecules. Cell. 2013;154(5):1151–61.
16. Seashore-Ludlow B, Rees MG, Cheah JH, Coko M, Price E V., Coletti ME, et al. Harnessing connectivity in a large-scale small-molecule sensitivity dataset. Cancer Discov. 2015;5(11):1210–23.
17. Barretina J, Caponigro G, Stransky N, Venkatesan K, Margolin AA, Kim S, et al. The Cancer Cell Line Encyclopedia enables predictive modelling of anticancer drug sensitivity. Nature. 2012 Mar;483(7391):603–7.
18. Mazumdar A, Tahaney WMWM, Reddy Bollu L, Poage G, Hill J, Zhang Y, et al. The phosphatase PPM1A inhibits triple negative breast cancer growth by blocking cell cycle progression. npj Breast Cancer. 2019 Dec 26;5(1):22.
19. Ma Y, Shepherd J, Zhao D, Bollu LR, Tahaney WM, Hill J, et al. SOX9 is essential for triple-negative breast cancer cell survival and metastasis. Mol Cancer Res. 2020;18(12).
20. Mi H, Huang X, Muruganujan A, Tang H, Mills C, Kang D, et al. PANTHER version 11: Expanded annotation data from Gene Ontology and Reactome pathways, and data analysis tool enhancements. Nucleic Acids Res. 2017;45(D1):D183–9.
21. Hafner M, Niepel M, Chung M, Sorger PK. Growth rate inhibition metrics correct for confounders in measuring sensitivity to cancer drugs. Nat Methods. 2016;13(6):521–7.
22. Bollu LR, Shepherd J, Zhao D, Ma Y, Tahaney W, Speers C, et al. Mutant P53 induces MELK expression by release of wild-type P53-dependent suppression of FOXM1. npj Breast Cancer. 2020 Dec 3;6(1):2.
23. Mazumdar A, Medina D, Kittrell FS, Zhang Y, Hill JL, Edwards DE, et al. The combination of tamoxifen and the rexinoid LG100268 prevents ER-positive and ER-negative mammary tumors in p53-null mammary gland mice. Cancer Prev Res. 2012;5(10):1195–202.
24. Zhang J-H. A Simple Statistical Parameter for Use in Evaluation and Validation of High Throughput Screening Assays. J Biomol Screen. 1999 Apr 1;4(2):67–73.
25. Hulsen T, de Vlieg J, Alkema W. BioVenn – a web application for the comparison and visualization of biological lists using area-proportional Venn diagrams. BMC Genomics. 2008;9(1):488.
26. Ma CX, Cai S, Li S, Ryan CE, Guo Z, Schaiff WT, et al. Targeting Chk1 in p53-deficient triple-negative breast cancer is therapeutically beneficial in human-in-mouse tumor models. J Clin Invest. 2012 Apr 2;122(4):1541–52.
27. Ma Z, Yao G, Zhou B, Fan Y, Gao S, Feng X. The Chk1 inhibitor AZD7762 sensitises p53 mutant breast cancer cells to radiation in vitro and in vivo. Mol Med Rep. 2012 Oct;6(4):897–903.
28. Hirai H, Iwasawa Y, Okada M, Arai T, Nishibata T, Kobayashi M, et al. Small-molecule inhibition of Wee1 kinase by MK-1775 selectively sensitizes p53-deficient tumor cells to DNA-damaging agents. Mol Cancer Ther. 2009 Nov 1;8(11):2992–3000.

29. Yang G-J, Zhong H-J, Ko C-N, Wong S-Y, Vellaisamy K, Ye M, et al. Identification of a rhodium(iii) complex as a Wee1 inhibitor against TP53-mutated triple-negative breast cancer cells. Chem Commun. 2018;54(20):2463–6.
30. Pellegata NS, Antoniono RJ, Redpath JL, Stanbridge EJ. DNA damage and p53-mediated cell cycle arrest: A reevaluation. Proc Natl Acad Sci U S A. 1996;93(26):15209–14.
31. Walerych D, Lisek K, Sommaggio R, Piazza S, Ciani Y, Dalla E, et al. Proteasome machinery is instrumental in a common gain-of-function program of the p53 missense mutants in cancer. Nat Cell Biol. 2016;18(8):897–909.
32. Strauss SJ, Higginbottom K, Jüliger S, Maharaj L, Allen P, Schenkein D, et al. The proteasome inhibitor bortezomib acts independently of p53 and induces cell death via apoptosis and mitotic catastrophe in B-cell lymphoma cell lines. Cancer Res. 2007;67(6):2783–90.
33. Pandit B, Gartel AL. Proteasome inhibitors induce p53-independent apoptosis in human cancer cells. Am J Pathol. 2011;178(1):355–60.
34. Lopes UG, Erhardt P, Yao R, Cooper GM. P53-Dependent Induction of Apoptosis By Proteasome Inhibitors. J Biol Chem. 1997;272(20):12893–6.
35. Meng X, Yang S, Li Y, Li Y, Devor EJ, Bi J, et al. Combination of proteasome and histone deacetylase inhibitors overcomes the impact of gain-of-function p53 mutations. Dis Markers. 2018;2018.
36. Verma N, Vinik Y, Saroha A, Nair NU, Ruppin E, Mills G, et al. Synthetic lethal combination targeting BET uncovered intrinsic susceptibility of TNBC to ferroptosis. Sci Adv. 2020 Aug 21;6(34):1–18.
37. Thompson LR, Oliveira TG, Hermann ER, Chowanadisai W, Clarke SL, Montgomery MR. Distinct TP53 Mutation Types Exhibit Increased Sensitivity to Ferroptosis Independently of Changes in Iron Regulatory Protein Activity. Int J Mol Sci. 2020 Sep 15;21(18).
38. Liu DS, Duong CP, Haupt S, Montgomery KG, House CM, Azar WJ, et al. Inhibiting the system xC–/glutathione axis selectively targets cancers with mutant-p53 accumulation. Nat Commun. 2017 Apr 28;8(1):1–14.

Figures

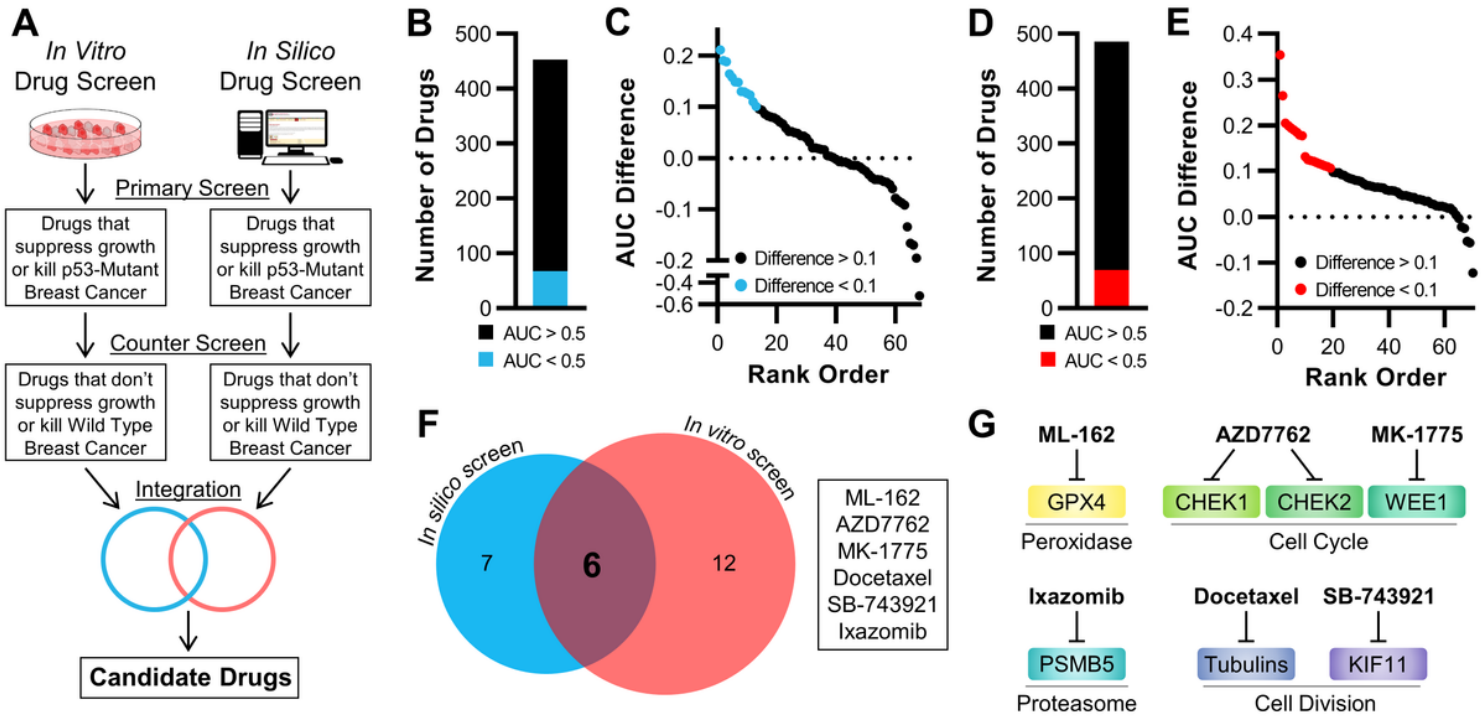

Figure 1

Integrative drug screening identifies drugs that induce death or suppress growth of p53-mutant breast cancers. (**A**) Workflow for integrated high-throughput drug screens. (**B**) Hits from primary *in vitro* screen. (**C**) Hits from counter *in vitro* screen. (**D**) Hits from primary *in silico* screen. (**E**) Hits from counter *in silico* screen. (**F**) Integration of *in vitro* and *in silico* drug screens and identified common drug hits. (**G**) Summary of identified candidate drugs, drug activity, and known protein targets (GPX4 – Glutathione Peroxidase 4; CHEK1 – Checkpoint Kinase 1; CHEK1 – Checkpoint Kinase 2; WEE1 – WEE1 G2 Checkpoint Kinase; PSMB5 – Proteasome 20S Subunit Beta 5; KIF11 – Kinesin Family Member 11).

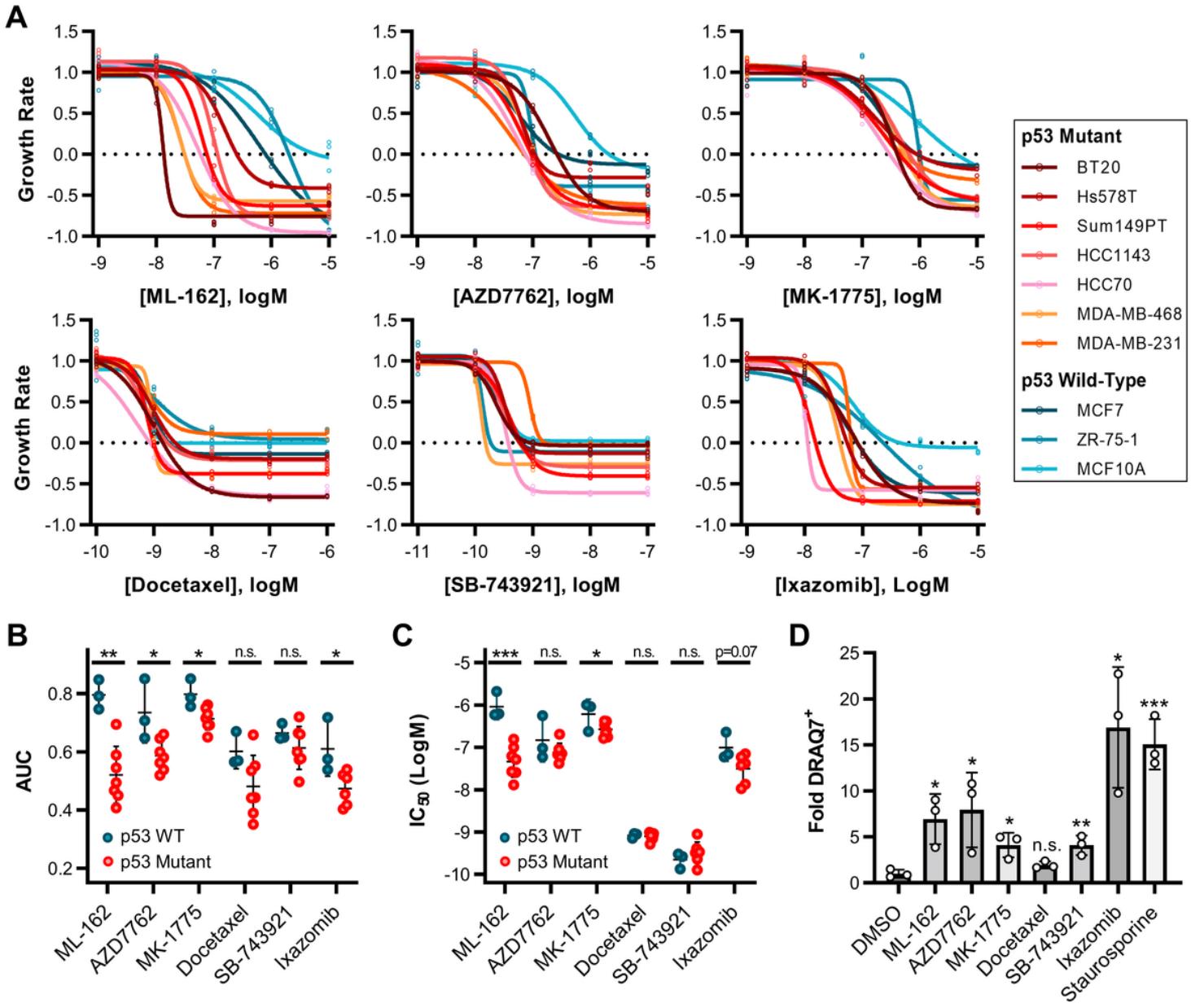

Figure 2

Confirmation of drug screen identifies ML-162 as inducing death in p53-mutant triple-negative breast cancer. (**A**) 5-log dose-response curves of identified drugs in p53-mutant (red/orange) and p53-wild type (blue) immortalized and cancerous breast cell lines (n=4). Comparison of (**B**) AUC and (**C**) IC_{50} values between p53-wild type and p53-mutant cells. (**D**) Fold $DRAQ7^{+}$ values for drug treated MDA-MB-468 cells, with staurosporine (1uM, 3Hr) as positive control (n=3). AUC and IC_{50} values were compared between p53 mutational statuses, and Fold $DRAQ7^{+}$ values were compared between drug and DMSO treatments, all with Student' *t*-test. For all comparisons, a *p*-value of < 0.05 was considered statistically significant. (*/**/*** = $p < 0.05/0.01/0.001$)

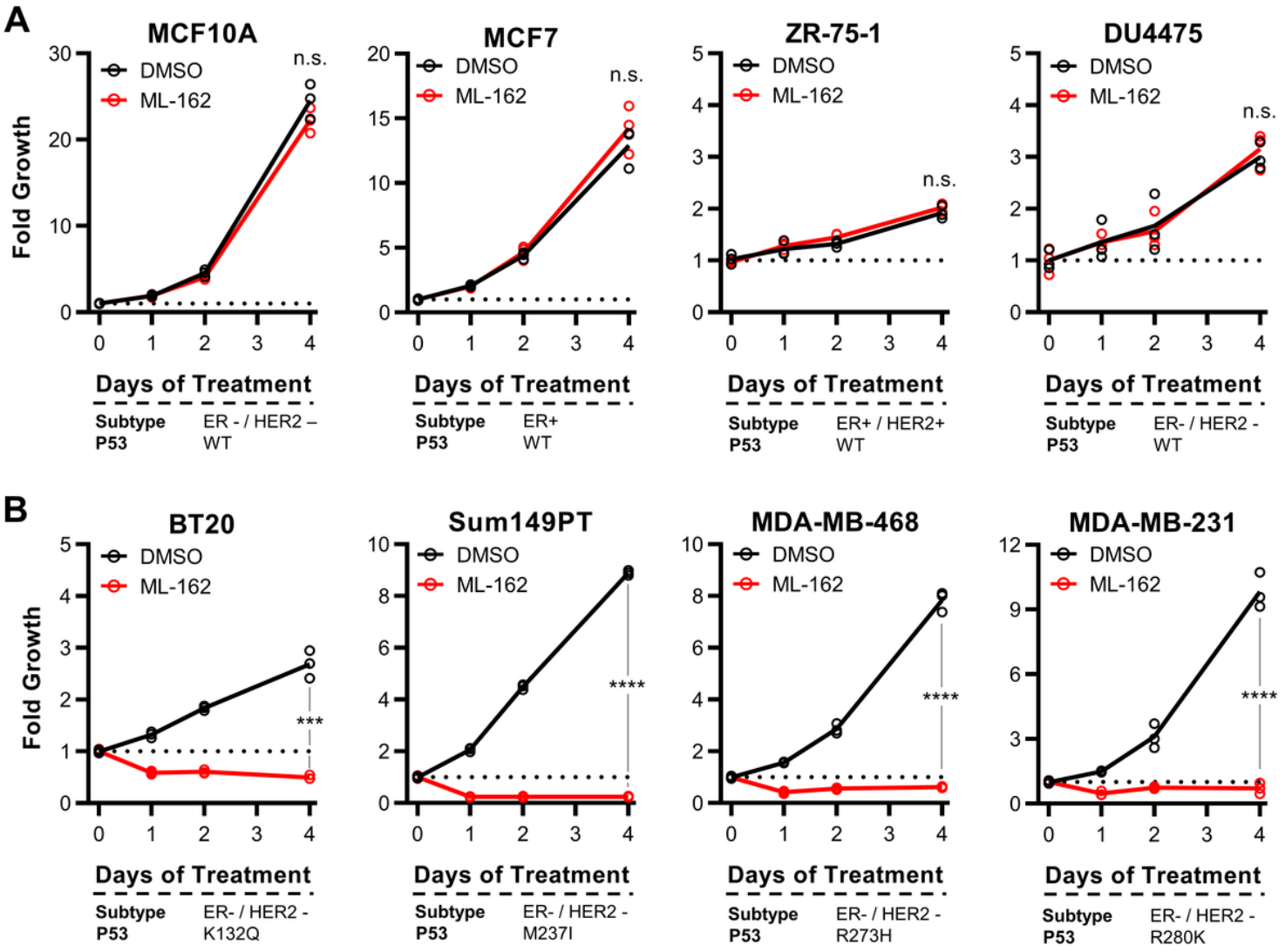

Figure 3

ML-162 exhibits preferential potency in p53-mutant triple-negative breast cancer. (**A**) Cell growth curves of p53-wild type immortalized breast and breast cancer cell lines in the presence of 100nM ML-162. (**B**) Cell growth curves of p53-mutant TNBC cell lines in the presence of 100nM ML-162. N=3 for all experiments. Fold growth of cells was compared using a mixed-effects model with Geisser-Greenhouse correction, and a $p < 0.05$ was considered statistically significant (***/**** = $p < 0.001/0.0001$).

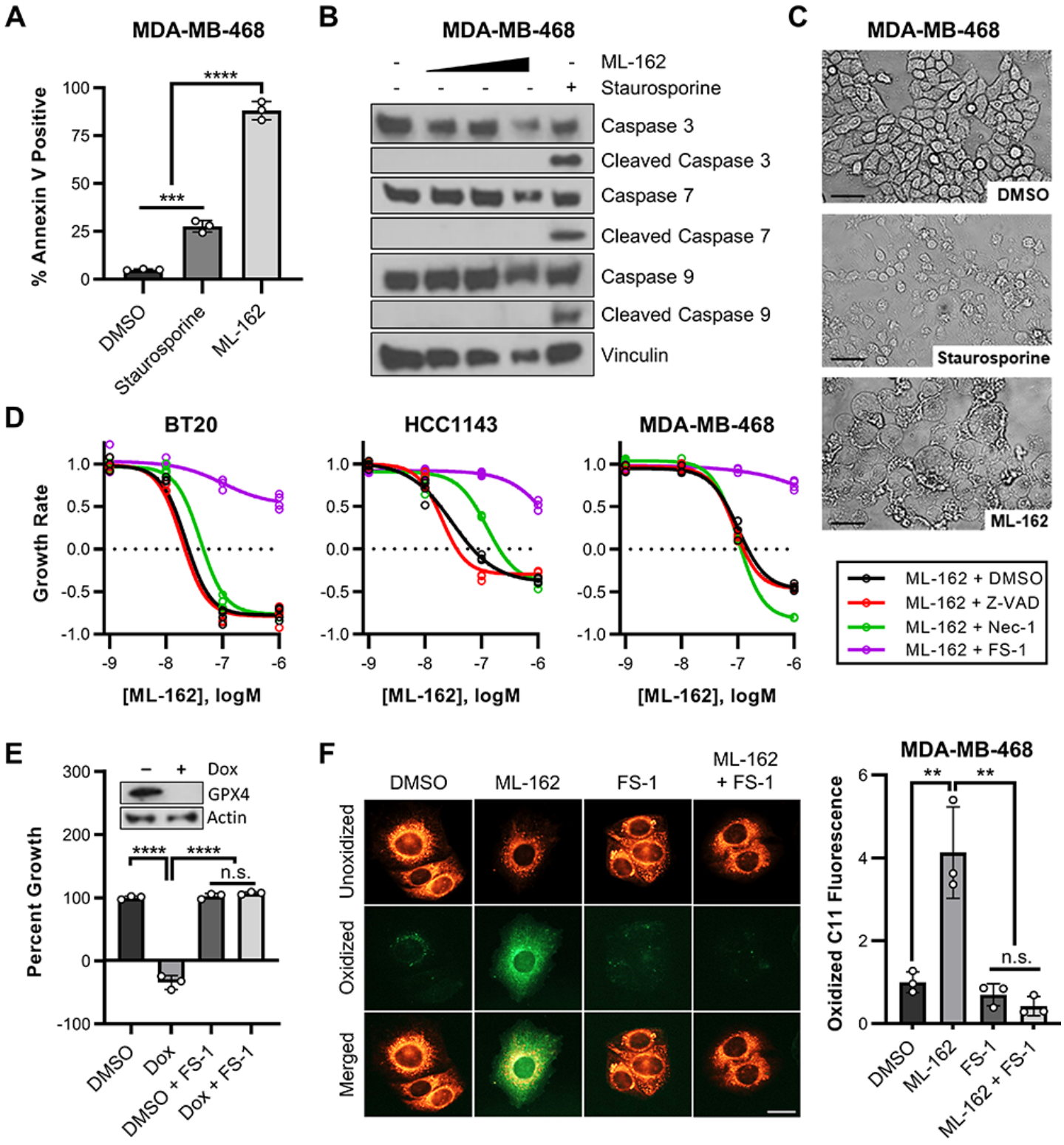

Figure 4

GPX4 inhibition induces ferroptosis in p53-mutant triple-negative breast cancer. (**A**) Quantification of Annexin V positivity after treatment with DMSO, Staurosporine (1uM, 3Hr), or ML-162 (500nM, 24Hr), and n=3. (**B**) Immunoblot of intact and cleaved caspases in MDA-MB-468 cells after treatment with DMSO, ML-162 (50, 100, 500nM), or Staurosporine (1uM, 3Hr). (**C**) Representative brightfield images of MDA-MB-468 after treatment with DMSO, staurosporine (1uM, 3Hr), or ML-162 (500nM, 24Hr). Scale bar = 50 μm.

(**D**) Growth rate of p53-mutant TNBC cell lines after co-treatment of ML-162 and death inhibitors (n=4). (**E**) Growth of MDA-MB-468 sgGPX4 cells with and without Dox and FS-1 co-treatment (n=3). Immunoblot demonstrates GPX4 knockout. (**F**) Representative images and quantification of C11-BODIPY$^{581/591}$ staining in MDA-MB-468 cells after treatment with ML-162 (100nM, 6Hr) and/or FS-1 (10uM, 24 Hr), and n=3. Scale bar = 20μm. Significance of differences between Annexin V positivity or C11 fluorescence was determined with Student's *t*-test. Fold growth of cells was compared using a mixed-effects model with Geisser-Greenhouse correction. For all comparisons, a *p*-value of < 0.05 was considered statistically significant (**/***/**** = $p < 0.01/0.001/0.0001$).

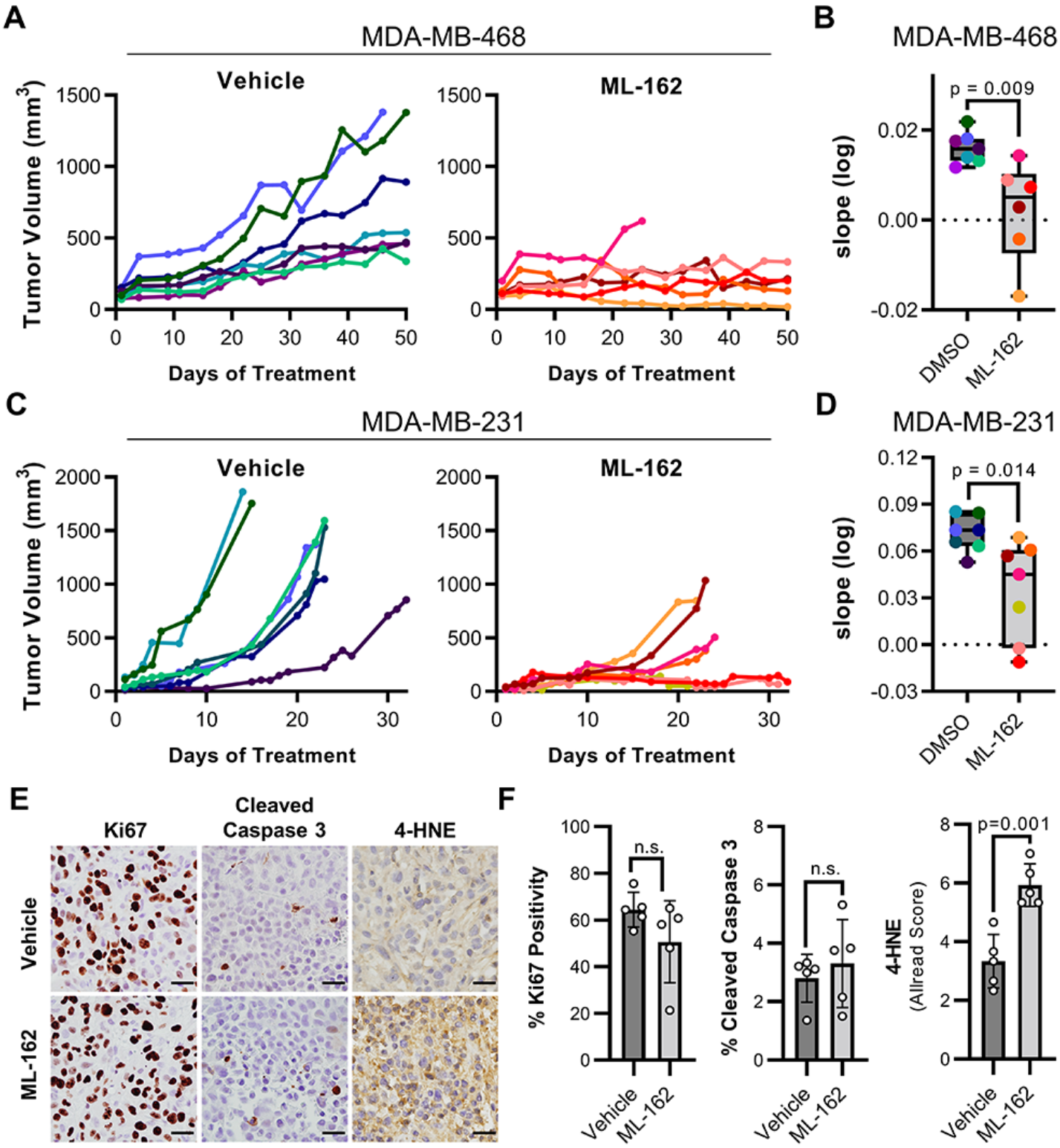

Figure 5

ML-162 reduces *in vivo* triple-negative breast cancer xenograft growth and induces lipid peroxidation. (**A**) Growth curves of MDA-MB-468 xenografts treated with vehicle (left) or ML-162 (right). (**B**) Analysis of MDA-MB-468 tumor growth slopes compared between DSMO and ML-162 treated tumors. (**C**) Growth curves of MDA-MB-231 xenografts treated with vehicle (left) or ML-162 (right). (**D**) Analysis of MDA-MB-231 tumor growth slopes compared between DSMO and ML-162 treated tumors. (**E**) Representative MDA-

MB-231 xenograft IHC images and quantification of Ki67, Cleaved Caspase 3, and 4-HNE staining after treatment with vehicle or ML-162. (**F**) Quantification of Ki67, Cleaved Caspase 3, and 4-HNE staining after vehicle or ML-162 treatment (n=5). Comparisons between vehicle and ML-162 treatment were compared with Student's *t*-test, and a *p*-value of < 0.05 was considered statistically significant.

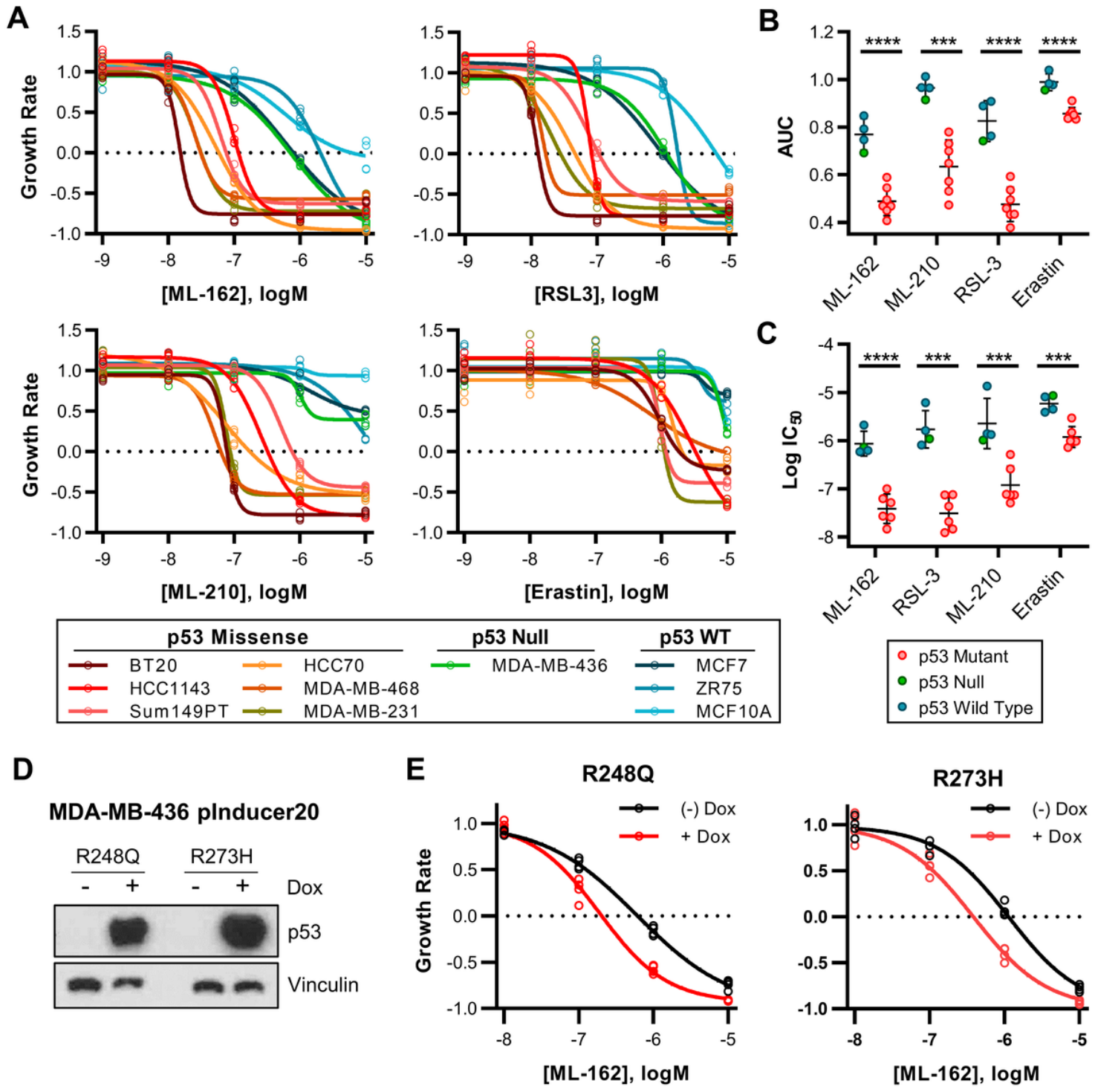

Figure 6

p53-missense mutants are preferentially sensitive to ferroptotic induction. (**A**) 5-log dose-response curves of GPX4 inhibitors ML-162, RSL3, ML-210, and System X_c inhibitor Erastin in p53-mutant (red/orange), p53-null (green) and p53-wild type (blue) immortalized breast and breast cancer cell lines (n=4). Comparison of (**B**) AUC and (**C**) IC_{50} values between p53-wild type/null and p53-mutant cells. (**D**) Immunoblot of p53 protein in MDA-MB-436 pInducer20 p53-R248Q and p53-R273H cell lines with and without Dox treatment. (**E**) Growth of MDA-MB-468 p53-R248Q and p53-R273H cells in the presence of ML-162 with and without Dox treatment (n=4). AUC and IC_{50} values were compared between p53 statuses with Student's *t*-test. For all comparisons, a *p*-value of < 0.05 was considered statistically significant. (***/**** = $p < 0.001/0.0001$)

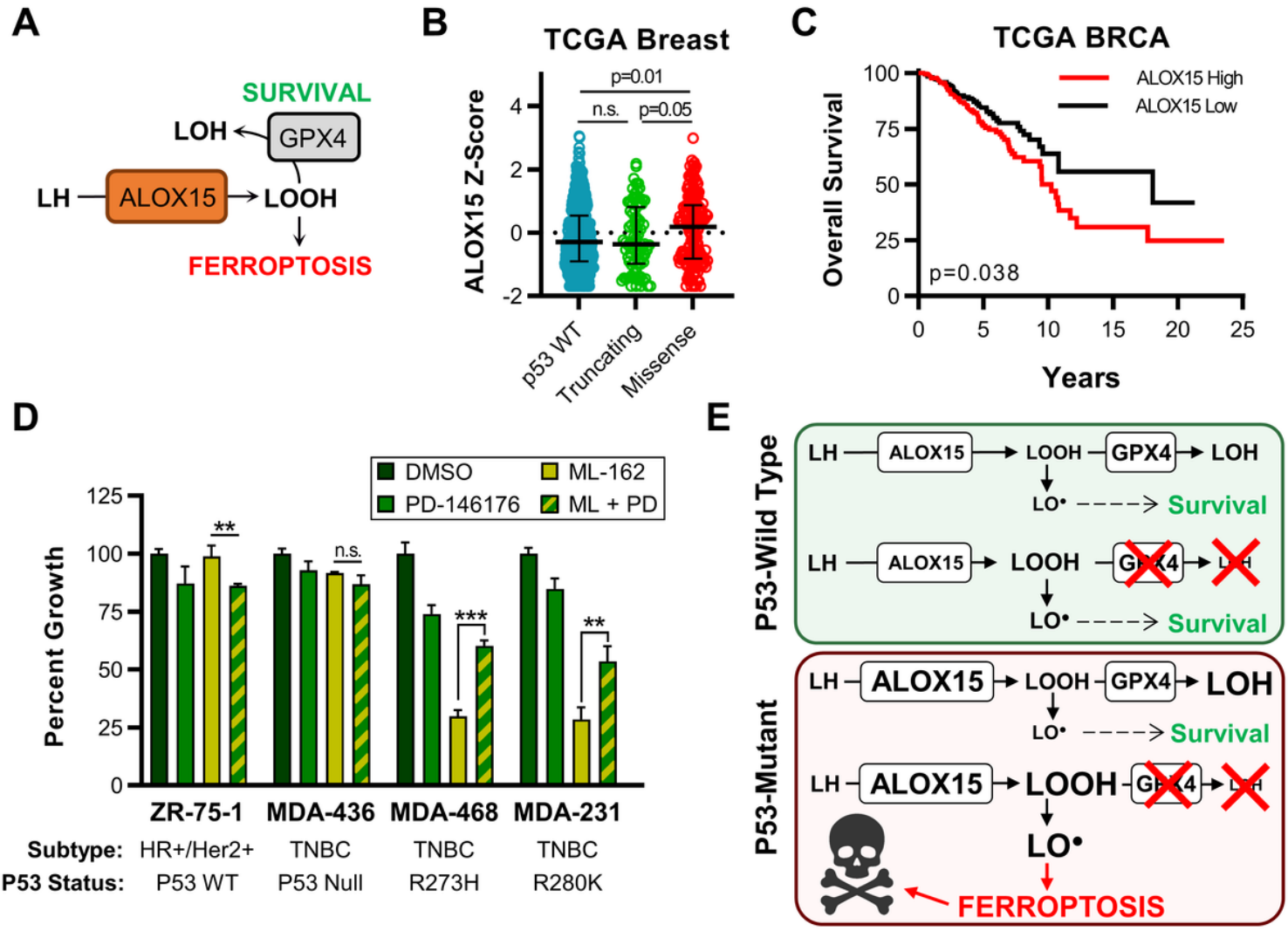

Figure 7

ALOX15 expression correlates with survival and ferroptotic sensitivity of p53-mutant breast cancer. (**A**) Schematic of ALOX15 biological activity. (**B**) mRNA expression of ALOX15 in the TCGA BRCA dataset, separated by p53 mutational status. (**C**) Overall survival of breast cancer patients in the TCGA BRCA

dataset based on ALOX15 expression. (**D**) Growth of breast cancer cells treated with DMSO, ALOX15 small molecule inhibitor PD-146176, and/or ML-162 (n=3). (**E**) Proposed mechanism of ferroptosis in p53-mutant breast cancer. Statistical significance of mRNA expression and percent growth differences were determined with Student's *t*-test. Kaplan-Meier curves were stratified by ALOX15 expression, dichotomized at median expression, and compared with Mantel-Cox log-rank analysis. For all comparisons, a *p*-value of < 0.05 was considered statistically significant (**/***, $p < 0.01/0.001$).

Supplementary Files

This is a list of supplementary files associated with this preprint. Click to download.

- BCRWesternBlots.pdf
- GPX4SupplementalFiguresV720220413.pdf
- SupplementaryTables20220314.xlsx